Signal, Image and Video Processing (2025) 19:289
https://doi.org/10.1007/s11760-025-03820-6

ORIGINAL PAPER

Methods for estimating full width at half maximum

Oona Rainio[1] · Johanna Hällilä[1] · Jarmo Teuho[1] · Riku Klén[1]

Received: 4 March 2024 / Revised: 28 November 2024 / Accepted: 4 January 2025

Abstract

Background: Measurement of full width at half maximum (FWHM) is used in multiple important applications related to the evaluation of the image resolution and the performance assessment of different scanner devices especially in positron emission tomography (PET) imaging, but little research has been performed about different methods for estimating FWHM. *Materials and methods*: We study seven different methods for estimating FWHM, including measuring FWHM according to its definition, four methods based on estimation of the standard deviation, the standard method of National Electrical Manufacturers Association (NEMA), and a new method utilizing an optimization algorithm to fit a Gaussian curve to the data. We compare their performance with several simulations. We also apply these techniques on two real data sets created by PET images of an ^{18}F-fluorodeoxyglucose resolution phantom imaged with High Resolution Research Tomograph concept camera and Biograph Vision Quadra and a sodium-22 point source imaged with RAYCAN X5 PET/CT system. *Results and conclusion*: According to our results from both simulated and real data, the most accurate methods are the first method based on the definition of FWHM and the NEMA standard method. In particular, both of these methods work in a reliable way in real data experiments, even when there is a very limited number of points available for FWHM computation.

Keywords Full width half maximum · Phantom imaging · Positron emission tomography

1 Introduction

Full width at half maximum (FWHM) is a measurement for characterizing the width of a peak of any curve resembling a Gaussian one. It is commonly used to study different topics in the field of spectroscopy, such as photoluminescence, lasers, and semiconductors [1–4]. It is also an important measure of quality of astronomical images [5, 6]. Thus, FWHM can be considered to be a widely used metric with multiple applications in multiple fields using different nuclear instruments.

Calculation of FWHM is also an essential method in assessment of performance in positron emission tomography (PET) imaging, with applications ranging from measurement of timing and energy resolution of detectors and assessment of the spatial resolution of complete PET imaging systems. In combined PET/computed tomography (CT) and PET/magnetic resonance imaging (MRI), measurement of FWHM is an integral part of the assessment of the resolution of PET imaging, and it is used as a common standard to study system-to-system performance [7–11].

The most intuitive and most common way to estimate FWHM is simply to measure the width of the curve at half of its total height. It is also possible to use a method based on estimating the standard deviation because it is known that the FWHM of a Gaussian curve formed out of observations from the normal distribution $\mathcal{N}(\mu, \sigma^2)$ is $\sigma\sqrt{8\ln 2}$. Alternatively, a Gaussian curve can be fit to the data with an optimization algorithm. Furthermore, National Electrical Manufacturers Association (NEMA) defines a method for estimation of FWHM [12].

However, there has not been new research assessing different methods for estimation of FWHM since the paper by Markevich and Gertner [13], which was published almost 40 years ago. Additionally, while Markevich and Gertner introduced five different methods for computing FWHM in [13], they only evaluated the methods with simulations and not

✉ Oona Rainio
ormrai@utu.fi

Johanna Hällilä
jokhal@utu.fi

Jarmo Teuho
jatateu@utu.fi

Riku Klén
riku.klen@utu.fi

[1] Turku PET Centre, University of Turku and Turku University Hospital, Turku, Finland

Published online: 13 February 2025

with empirical data. Due to the lack of further research, neither the current NEMA standard method nor any approach based on optimization have been compared with the methods in [13]. In majority of the applied research, only the FWHM values given by the NEMA method are typically considered, if the FWHM method is even specified.

Here, we introduce seven different methods for estimating the FWHM and compare their performance by using simulated and empirical data. In particular, we study how the number of original observations, the number of points used to plot the curve, and different error terms affect our results. We also test our methods from real data sets from two clinical and one preclinical PET systems with different resolution characteristics. The data was obtained by imaging a resolution phantom injected with ^{18}F-fluorodeoxyglucose (^{18}F-FDG) on a dedicated high-resolution brain PET system and a novel total-body PET system. Finally, a sodium-22 (^{22}Na) point source was collected to evaluate the methods on a high-resolution preclinical imaging system.

2 Methods

We present here the original methods F1-F5 proposed by Markevich and Gertner [13], the NEMA standard method (named here F6), and our new method F7 based on the use of an optimization algorithm to fit a Gaussian curve to the data. More detailed information about all the methods can be found in the code (see the link in Code and data availability statement).

Suppose that there is a data set Z consisting of numerical samples. For an integer n much less than the sample size of Z, choose $n+1$ numbers k_i such that $k_i < k_{i+1}$ for $i = 1, \ldots, n$. Define then vectors x and y of length n so that $x_i = (k_i + k_{i+1})/2$ and $y_i = \#\{z \in Z \mid k_i \le z < k_{i+1}\}$ for $i = 1, \ldots, n$, where $\#S$ denotes the number of elements in the set S. Now, the curve defined by the points (x_i, y_i), $i = 1, \ldots, n$, is a summary of the information in the original data Z. Denote below $N = \sum_{i=1}^{n} y_i$, which is equivalent to the size of Z if all the observations lie between k_1 and k_{n+1}.

Method F1. Let $j = 1, \ldots, n$ be the index of the middlemost maximum of y. Fix l and r as the closest indexes i on each side of j with count y_i less than half of y_j or, equivalently, $l = \max\{i = 1, \ldots, j-1 \mid y_i < y_j/2\}$ and $r = \min\{i = j+1, \ldots, n \mid y_i < y_j/2\}$. By linear interpolation, we can estimate that the intersection points of the curve and the horizontal line at half maximum are

$$\begin{aligned} c_l &= x_l + \frac{y_j/2 - y_l}{y_{l+1} - y_l}(x_{l+1} - x_l), \\ c_r &= x_r - \frac{y_j/2 - y_r}{y_{r-1} - y_r}(x_r - x_{r-1}). \end{aligned} \tag{1}$$

The FWHM given by this method is the difference $c_r - c_l$.

Method F2. Fix j as in F1 and return the FWHM as

$$\sqrt{\frac{8\ln 2}{2\pi}}\frac{N}{y_j}\left(\frac{x_j + x_{j+1}}{2} - \frac{x_{j-1} + x_j}{2}\right).$$

This method is based on the fact that the maximum height of the Gaussian curve is $1/(\sigma\sqrt{2\pi})$ when the area under the curve is 1. Consequently, we can use the height of our curve to estimate the standard deviation σ. To find the correctly scaled height, the maximum value y_j needs to be divided by both the width of the jth interval and total number of observations N as the counts describe the area on the intervals. The expression above is obtained when the solved value of σ is input into the formula $\sigma\sqrt{8\ln 2}$ of the FWHM.

Method F3. From each count and the midpoint of the corresponding interval, calculate the sums $T_1 = \sum_{i=1}^{n} x_i y_i$ and $T_2 = \sum_{i=1}^{n} x_i^2 y_i$, use the estimate $\sigma_3 = \sqrt{T_2/N - (T_1/N)^2}$ for the standard deviation, and compute FWHM as $\sigma_3\sqrt{8\ln 2}$.

Method F4. Fit a parabola with parameters a, b, c to logarithmic counts so that $\ln(y_i) \sim ax_i^2 + bx_i + c$ for $y_i > 3$, use the estimate $\sigma_4 = \sqrt{-1/(2a)}$, and return the FWHM as the value $\sigma_4\sqrt{8\ln 2}$. The reasoning behind this method follows from the formula of the Gaussian function

$$f(x|\mu,\sigma) = \frac{1}{\sigma\sqrt{2\pi}}e^{-\frac{1}{2}\left(\frac{x-\mu}{\sigma}\right)^2}. \tag{2}$$

The reason why the observations $y_i \le 3$ are not taken into account in this method nor the next is that they would be too sensitive to error otherwise.

Method F5. Remove all the observations (x_i, y_i) such that $y_i \le 3$ and fit the line

$$\frac{\ln(y_{i+1}/y_{i-1})}{x_{i+1} - x_{i-1}} \sim Ax_i + B$$

to the remaining data, use the estimate $\sigma_5 = \sqrt{1/|A|}$, and return the FWHM as the value $\sigma_5\sqrt{8\ln 2}$. The justification of this method also comes from the Gaussian function in (2).

Method F6. This method is given by NEMA in [12, p. 10]. First, fix j as in F1 and find the unique solution for the parabola passing through the three points around this maximum: $y_i \sim ax_i^2 + bx_i + c$ for $i = j-1, j, j+1$. The height of this parabola is $h = -b^2/(4a) + c$. In the special case $a = 0$, let $h = y_j$ instead. Fix then $l_h = \max\{i = 1, \ldots, j-1 \mid y_i < h/2\}$ and $r_h = \min\{i = j+1, \ldots, n \mid y_i < h/2\}$. Use then these values l_h and r_h to find the points of the curve at the height of $h/2$ by replacing y_j, r, l with h, r_h, l_h, respectively, in (1), and return FWHM as their difference.

Method F7. This final method is based on our idea and can potentially be seen as an improvement or further development of the method F3. First, scale the vector y by dividing

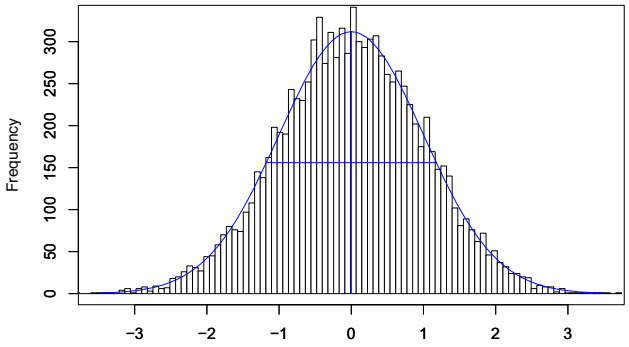

Fig. 1 One simulated data set of $N = 10,000$ observations generated from the standard normal distribution $\mathcal{N}(0, 1)$ as a histogram with $n = 100$ intervals of length 0.0781. The Gaussian curve obtained from the formula (2) with $\mu = 0$ and $\sigma = 1$ and scaled to suitable height by using the coefficient $0.0781N$ is plotted in blue. The horizontal and vertical line segments for measuring FMWH and the height of the Gaussian curve are also denoted in blue

it with the factor $N/(n-1) \cdot \sum_{i=1}^{n-1}(x_i - x_{i+1})$ so that the area under the curve is approximately 1. Let this new scaled vector be y'. Create a cost function that, when given the vector $A = (A_1, A_2, A_3)$ and the vector x, computes the squared error $\sum_{i=1}^{n}(f(x_i|A_2, A_3) + A_1 - y_i')^2$, where f is the Gaussian function in (2). Initialize the vector A so that $A_1 = 0$, $A_2 = T_1'/N'$, and $A_3 = \sqrt{T_2'/N' - (T_1'/N')^2}$, where $N' = \sum_{i=1}^{n} y_i'$ and T_1', T_2' are the sums T_1, T_2 computed as in F3 but for the scaled vector y_i'. Use an optimization algorithm with this cost function to find to fit the best possible parameters A for fitting a Gaussian curve to the data (x_i, y_i'). Finally, return FWHM as $\sigma_7\sqrt{8\ln 2}$, where σ_7 is the standard deviation of the fitted curve.

2.1 Simulations

To test these methods, we performed the following experiment: A data set Z is of N observations is generated from the standard normal distribution $\mathcal{N}(0, 1)$ and divided into n intervals of length $(\max(Z) - \min(Z))/n$ to obtain points (x_i, y_i) for $i = 1, \ldots, n$. The simulation is repeated for 1000 times for each choice of n and N to compute the mean relative error of each method. Regardless of choices of other parameters, the ground-truth FWHM in these simulations is $\sqrt{8\ln 2} \approx 2.355$ because we have $\sigma = 1$ in the standard normal distribution. To study the impact of error, we add either noise from the uniform distribution $U(-s/2, s/2)$ to the original observations $z \in Z$ or noise from the normal distribution $\mathcal{N}(0, t^2)$ to the points y_i. Note that in the latter case the number N of generated observations in Z does not coincide with the sum $N = \sum_{i=1}^{n} y_i$ used to in the methods F1–F7. An example of the data points generated by the simulation is shown in Fig. 1.

2.2 Estimation of the FWHM from the simulations

The value of FWHM is estimated with each method F1–F7. These methods are evaluated by considering the difference between the estimated FWHM and the ground-truth FWHM equal to $\sqrt{8\ln 2}$. The absolute value of this difference divided by the real FWHM is the relative error.

In our simulations, we first evaluated the methods in 1000 simulations where $N = 1,000,000$ normally distributed observations are divided onto $n = 100$ intervals of equal length. For each method, a one-sided t-test was also performed to find out whether the real mean of the distribution of the differences between the estimated and the real FWHM is 0. A paired t-test was performed to see if the differences between the two best performing methods were significant or not. A p-value<0.05 was used to denote statistical significance. The simulations are then studied for various values of n and N, and also in the cases where noise is added with some s or t. The computations required by both of these simulations and the real data experiments below are executed with programming language R [14].

2.3 Phantom imaging

A resolution phantom injected with 218.6 MBq ^{18}F-FDG was imaged with High Resolution Research Tomograph (HRRT) concept camera (Siemens, Erlangen, Germany) and PET/CT scanner Biograph Vision Quadra (Siemens Healthineers). The HRRT represents a high-resolution dedicated brain imaging system with resolution up to 2–3 mm [15], whereas the Quadra represents a total body imaging system with a resolution of 3–6 mm [16]. As shown in Supplement Fig. 1, the resolution phantom has cylindrical cavities with a diameter of 5 mm, 4 mm, 3 mm and 2 mm which are filled with radioactivity.

The resulting images were analyzed with Carimas [17]. Line profiles were drawn above the hot cavities on line segments (Supplement Figure 2) within the phantom containing ^{18}F-FDG (Fig. 2) and in [18]. The data points of the peaks in the line profile representing hot cavities were separated from each other with vertical lines in 2D plots. Only the data of the holes with a diameter of 5 mm were included in the comparison. The final data contained 8 sets of 29–39 coordinate points corresponding four imaging times of two PET scanners so that the distance between the x-coordinates of two adjacent points was always 0.5 mm. More technical details of phantom imaging and image reconstruction are given in Supplement, section Resolution Phantom imaging with the Quadra and HRRT. The FWHM was estimated from these peaks with methods F1–F7 from and the mean values were computed from each set of estimates.

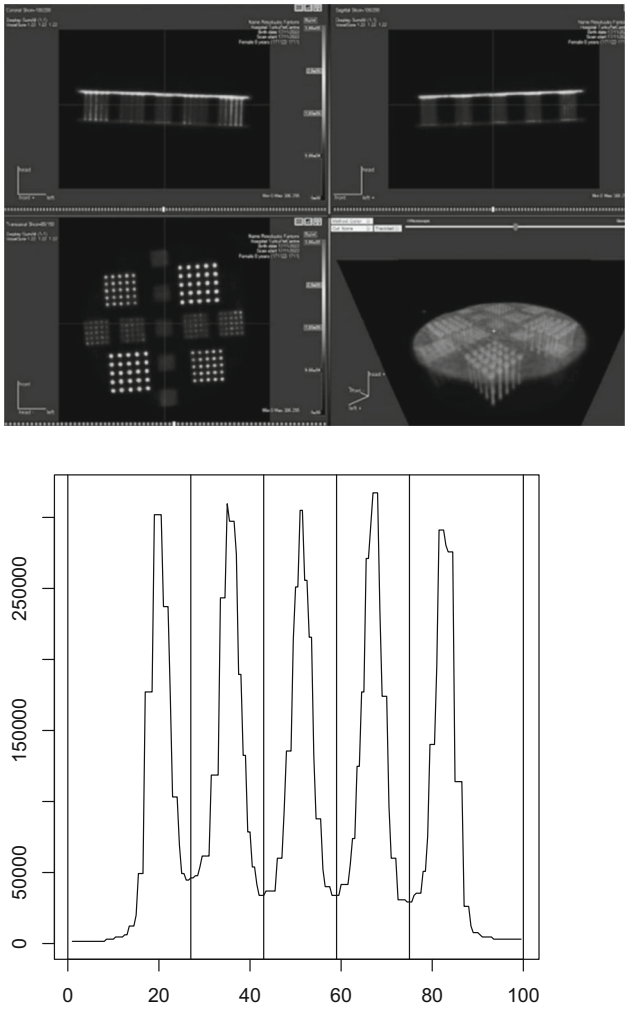

Fig. 2 A PET image of resolution phantom in Carimas and a plot depicting the five concentration peaks with vertical lines separating them from each other (unit of x-axis is mm)

2.4 Point source measurements

The point source measurements were performed using a ^{22}Na point source embedded in a $1 \times 1 \times 1\text{cm}^3$ acrylic cube (Eckert and Ziegler, Valencia, CA), which was imaged with the RAYCAN X5 preclinical PET/CT system (RAYCAN Technology Co., Ltd. Shuzou, China) which has resolution characteristics of 1–2 mm. The active diameter of the source was 0.25 mm with an activity of 0.342 MBq at the time of the measurement. The image reconstruction resulted to a static PET image visualizing the point source. Data was extracted from the point source images by drawing of point source response functions in axial, radial, and tangential directions and summing of 1D profiles drawn parallel to the direction of the measurement. Additional information can be read from Supplement, section Point-source measurements on the pre-clinical system. The FWHM was estimated from the data points for each direction separately.

Table 1 The mean and the standard deviation (Sd) of the differences between the estimated and the real FWHM, the mean absolute error (MAE), and the mean relative error (MRE) for each method F1–F7 in 1000 simulations of $N = 100,000$ normally distributed observations divided into $n = 100$ intervals

	Mean	Sd	MAE	MRE
F1	−0.0224	0.0309	0.0304	1.29%
F2	−0.0313	0.0255	0.0337	1.43%
F3	4.65e–4	0.00539	0.00430	0.183%
F4	0.0161	0.0170	0.0190	0.808%
F5	0.0619	0.0487	0.0667	2.83%
F6	−0.0244	0.0310	0.0316	1.34%
F7	6.96e–4	0.00743	0.00604	0.256%

3 Results

As can be seen from Table 1, the methods F3, F7, and F4 performed the best with mean relative errors less than 1% whereas F5 produced the most error. According to the paired t-test, the relative errors of the best performing methods F3 and F7 were already statistically significant (p-value $< 2.2e-16$). The p-values of the one-sided t-tests were less than or equal to 0.003122, so the real mean of the distribution of the differences between the estimated and the real FWHM is not equal to 0 for any of the methods.

The impact of both the number of intervals n and the observations N was also inspected. As can be seen from Fig. 3, the methods F3 and F7 produced considerably less error than others for small values of N and for high values of n. This would indicate that these methods can be considered reliable with sparse data, as long as the data sampling is sufficient. If the value of the quotient $n/N > 1/10$, all the other methods have mean relative error over 5% and some of them, especially F1 and F6, are very unreliable.

Table 2 contains the mean values of the methods F1–F7 used to estimate the FWHM of the ^{18}F-FDG concentration peak in the holes with diameter of 5 mm in the resolution phantom for different cameras and imaging times. We see that methods F1, F2, and F6 result in mean values close to 5 mm, while F3–F5 and F7 give too high estimates. If 5 mm is considered the ground-truth value, then the most accurate method is F6 with mean relative errors of 9.07-−10.6% for HRRT and 15.4-−15.5% for Quadra. As HRRT has smaller FWHM measurements than Quadra according to every method, they would all result in the same conclusion about the relative performance of these two scanners.

Table 3 contains FWHM estimates from the point source from different three directions (axial, radial, tangential). It is not known what the exact ground-truth FHWM should be but, based on the size of the detector of the camera and the method of reconstruction, a reasonable FWHM value would

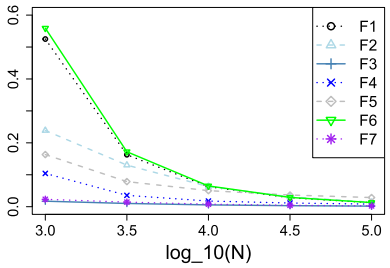

(a) No error term added.

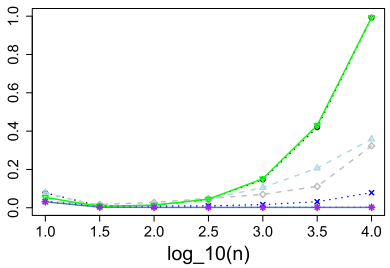

(b) No error term added.

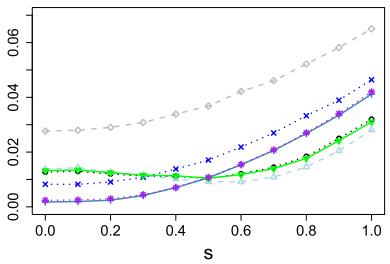

(c) $n = 100$, $N = 100,000$, error generated from $U(-s/2, s/2)$.

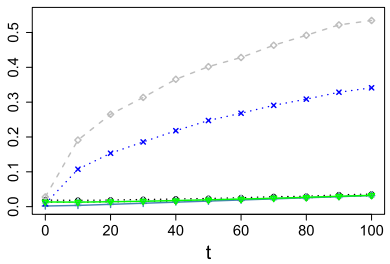

(d) $n = 100$, $N = 100,000$, error from the normal distribution $\mathcal{N}(0, t^2)$.

Fig. 3 The mean relative errors of methods F1–F7 computed from 1000 simulations of N normally distributed observations divided into n intervals when the number n of intervals, the number N of observations, and the errors are as in the sub-captions. The colors, point symbols, and line styles for the methods in each four plots are the same (see the legend of the first one). The y-axis expresses the mean relative error as a numeric value instead of a percentage like in Table 1

be around 1–2 mm. We see that the methods F1, F6, and F7 produce estimates less than 3 mm, while F3-F5 return clearly too high values.

Table 2 Mean values of the estimates (mm) given by the seven methods computed from phantom imaging with different scanners and imaging times (min)

HRRT							
Time	F1	F2	F3	F4	F5	F6	F7
15	5.23	5.79	8.47	29.5	22.8	5.21	12.8
30	5.30	5.82	8.49	29.6	22.8	5.28	12.8
60	5.28	5.79	8.49	29.7	22.9	5.27	12.8
120	5.21	5.75	8.45	30.0	22.8	5.20	12.7
Quadra							
Time	F1	F2	F3	F4	F5	F6	F7
35	5.64	6.40	9.35	30.4	24.0	5.63	16.5
76	5.64	6.40	9.33	30.5	24.0	5.63	16.5
190	5.64	6.39	9.33	30.5	23.9	5.63	16.4
360	5.64	6.37	9.33	30.6	23.9	5.63	16.4

Table 3 Estimates (mm) of FWHM obtained with the seven methods by imaging the sodium-22 point source from three directions

	Axial	*Radial*	Tangential
F1	1.34	2.15	2.30
F2	1.51	3.34	3.02
F3	2.34	30.9	27.9
F4	17.1	48.9	69.6
F5	24.9	84.3	449
F6	1.34	2.09	2.27
F7	1.47	2.85	2.87

4 Discussion

We evaluated altogether seven methods for estimating the FWHM from simulated and empirical data collected from three PET systems. The analysis revealed differences between the methods in terms of data sampling frequency, data distribution, and the effect of noise in simulated and empirical data. The evaluation revealed that only a few of the methods work reliably on both simulated and empirical data while some of them are very sensitive to noise.

The most simple method, F1, performs decently in the simulations and with empirical data. It was one of the more reliable methods when it comes to the real data experiment. Out of the methods based on estimation of the standard deviation, F3 is often the best in simulations, as was noted also in [13], while F4 and F5 in particular perform very poorly on the real data, probably due to the fact that they are prone to errors when there is not enough data points to reliably estimate the standard deviation. The methods F4 and F5 seem also to be sensitive to noise, which always exists in real data and the same trend can be seen in our empirical measurements. The NEMA standard method F6 performs well in simulations and gave the best performance for real data.

F7 was a new method suggested in this paper, to indicate possible improvement of F3. According to the results, F3 performs only slightly better in all simulations except the last one in which we added normally distributed errors to the counts of the intervals creating the curve. In the real data experiments, F3 also performed better for phantom imaging but, unlike F7, it produced unrealistically high estimate for the point source measurement from the radial direction.

The possible explanation for why F7 performed worse for the phantom imaging might be that there are too many data points close to zero on each side of the peak and they had too high impact of the resulting estimate. Given the method assumes that the distribution of the data resembles a Gaussian curve and tries to fit a Gaussian curve to the data, reduced accuracy is expected in cases when the data distribution is not purely Gaussian, the data is skewed, or it contains tails either left or right of the distribution.

In essence, estimating the FWHM often depends on how well the data is represented by a Gaussian distribution. If it is not, then the estimate can produce large errors. Due to the presence of background, the F6 method by NEMA effectively excludes longer tails in the data, and fits only the peak. The FWHM estimation from the data with F7 can therefore be inconsistent with F6. However, despite the differences between these methods, they all gave the HRRT camera smaller FWHM values than Quadra, which is the correct result based on earlier research about these cameras [15, 16].

We had a limited number of simulations and real data experiments, so future research is warranted. One possible focus of further study would be to inspect what happens if the number of data points of the curve is increased with some interpolation method. In our first real data experiment with the HRRT and Quadra, the adjacent concentration peaks are slightly fused with each other (see the right half of Fig. 2) so their real height cannot be properly calculated. Since this issue–related to intrinsic partial volume effects as well as the point spread function of the PET system - is often present with real data, it might be interesting to test whether adding data points to the separated curves would affect the performance of methods. Additionally, our current study can be expanded to focus on applications on different fields in the future.

5 Conclusion

Based on our simulations and real data experiments, we would recommend using either the NEMA standard method F6 [12], or the method of simply measuring the width of the peak at the half of its maximum height (introduced as F1 in [13]). This study confirms that these well-established methods commonly used for FWHM measurements produce accurate estimates in both simulated and real data and can be reliably used for measuring FWHM. The method F7 introduced in this paper of fitting a Gaussian curve to the data points with an optimization algorithm for the estimation of FWHM showed promise in simulated data, but had poorer performance when evaluated with empirical data.

Supplementary Information The online version contains supplementary material available at https://doi.org/10.1007/s11760-025-03820-6.

Funding Open Access funding provided by University of Turku (including Turku University Central Hospital). The first author was financially supported by the Finnish Culture Foundation. This study was supported through funding from State Research Funding (the expert responsibility area (ERVA) of Turku University Hospital), by the clinical EVO Grant admitted by Turku PET Centre (Project Number: 13720).

Code and data availability Available at https://github.com/rklen/FWHM_methods.

Declarations

Conflict of interest On behalf of all authors, the corresponding author states that there is no Conflict of interest.

References

1. Chen, F., Itagi, A., Bain, J., Stancil, D., Schlesinger, T., Stebounova, L., Walker, G., Akhremitchev, B.: Imaging of optical field confinement in ridge waveguides fabricated on very-small-aperture laser. Appl. Phys. Lett. **83**(16), 3245–3247 (2003)
2. Chiangga, S., Suwanarat, S., Phatharacorn, P., Yupapin, P.: Supercontinuum generation of an optical pulse in a silicon micro-ring resonator. Opt. Quant. Electron. **48**, 1–13 (2016)
3. Nakamura, S., Mukai, T., Senoh, M.: Candela-class high-brightness ingan/algan double-heterostructure blue-light-emitting diodes. Appl. Phys. Lett. **64**(13), 1687–1689 (1994)
4. Wu, J., Yaguchi, H., Onabe, K., Ito, R., Shiraki, Y.: Photoluminescence properties of cubic gan grown on gaas (100) substrates by metalorganic vapor phase epitaxy. Appl. Phys. Lett. **71**(15), 2067–2069 (1997)
5. Anisimova, E., Bednář, J., Páta, P.: Efficiency of wavelet coefficients thresholding techniques used for multimedia and astronomical image denoising. In: 2013 International Conference on Applied Electronics, pp. 1–4 (2013). IEEE
6. Cvetojevic, N., Lawrence, J., Ellis, S., Bland-Hawthorn, J., Haynes, R., Horton, A.: Characterization and on-sky demonstration of

an integrated photonic spectrograph for astronomy. Opt. Express **17**(21), 18643–18650 (2009)
7. Delso, G., Fürst, S., Jakoby, B., Ladebeck, R., Ganter, C., Nekolla, S.G., Schwaiger, M., Ziegler, S.I.: Performance measurements of the siemens mmr integrated whole-body pet/mr scanner. J. Nucl. Med. **52**(12), 1914–1922 (2011)
8. Lodge, M.A., Leal, J.P., Rahmim, A., Sunderland, J.J., Frey, E.C.: Measuring pet spatial resolution using a cylinder phantom positioned at an oblique angle. J. Nucl. Med. **59**(11), 1768–1775 (2018)
9. Lodge, M.A., Rahmim, A., Wahl, R.L.: A practical, automated quality assurance method for measuring spatial resolution in pet. J. Nucl. Med. **50**(8), 1307–1314 (2009)
10. Rausch, I., Cal-González, J., Dapra, D., Gallowitsch, H.J., Lind, P., Beyer, T., Minear, G.: Performance evaluation of the biograph mct flow pet/ct system according to the nema nu2-2012 standard. EJNMMI Phys. **2**, 1–17 (2015)
11. Spencer, B.A., Berg, E., Schmall, J.P., Omidvari, N., Leung, E.K., Abdelhafez, Y.G., Tang, S., Deng, Z., Dong, Y., Lv, Y., et al.: Performance evaluation of the uexplorer total-body pet/ct scanner based on nema nu 2–2018 with additional tests to characterize pet scanners with a long axial field of view. J. Nucl. Med. **62**(6), 861–870 (2021)
12. National Electrical Manufacturers Association, N.N.: Performance Measures of Positron Emission Tomographs (2013)
13. Markevich, N., Gertner, I.: Comparison among methods for calculating fwhm. Nuclear Instrument Methods Phys Res Sect A Accelerators Spectrometers Detectors Assoc Equipment **283**(1), 72–77 (1989)
14. Team, R.C.: R: A language and environment for statistical computing, r foundation for statistical computing (2020)
15. De Jong, H.W., Van Velden, F.H., Kloet, R.W., Buijs, F.L., Boellaard, R., Lammertsma, A.A.: Performance evaluation of the ecat hrrt: an lso-lyso double layer high resolution, high sensitivity scanner. Phys. Med. Biol. **52**(5), 1505 (2007)
16. Prenosil, G.A., Sari, H., Fürstner, M., Afshar-Oromieh, A., Shi, K., Rominger, A., Hentschel, M.: Performance characteristics of the biograph vision quadra pet/ct system with a long axial field of view using the nema nu 2–2018 standard. J. Nucl. Med. **63**(3), 476–484 (2022)
17. Rainio, O., Han, C., Teuho, J., Nesterov, S.V., Oikonen, V., Piirola, S., Laitinen, T., Tättäläinen, M., Knuuti, J., Klén, R.: Carimas: an extensive medical imaging data processing tool for research. J. Digit. Imaging **36**(4), 1885–1893 (2023)
18. Hällilä, J.: Cross-calibration of human PET scanners with phantom studies. Master's thesis, University of Turku (2023)